Young Researcher Award of The Electrochemical Society of Japan (Sano Award)

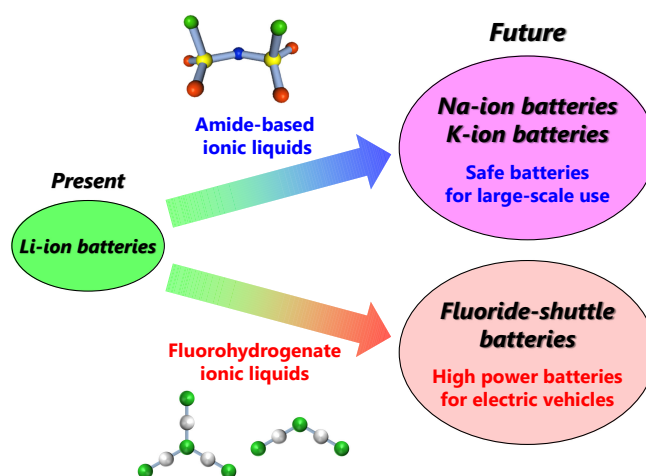# Next-generation Rechargeable Batteries Utilizing Ionic Liquids and Various Charge Carriers

Takayuki YAMAMOTO*,§ (ID)

Institute of Advanced Energy, Kyoto University, Gokasho, Uji, Kyoto 611-0011, Japan

* Corresponding author: yamamoto.takayuki.2w@kyoto-u.ac.jp

OPEN ACCESS

ABSTRACT

Renewable energy resources and rechargeable batteries are key to establishing a carbon-neutral society. Lithium-ion batteries (LIBs) have been widely used in portable electronic devices for the past 30 years. However, the further spread of large-scale batteries is essential in the household and industrial sectors, which drives the research and development of technologies beyond LIBs. Since ionic liquids are safe and confer unique physicochemical properties, several next-generation batteries utilizing ionic liquid electrolytes have been researched. Sodium-ion and potassium-ion batteries show promise in overcoming the potential problems of LIBs related to the uneven distribution of lithium and cobalt resources. Fluoride-shuttle batteries deliver significantly higher theoretical energy densities compared to current LIBs. Nevertheless, many issues remain unresolved for the practical application of these batteries. This comprehensive paper provides several research topics on next-generation rechargeable batteries utilizing ionic liquids and various charge carriers, unveiling their novelty, the issues to be solved, and future research directions.

1. Introduction

Rechargeable batteries are indispensable in modern society, with applications from portable electronic devices to stationary use. Lithium-ion batteries (LIBs) have been applied to small-sized devices, such as smartphones and personal computers, because of their superior energy densities compared to existing practical batteries. The demand for large-sized LIBs is also currently increasing; they have been considered for use in combination with intermittent renewable energy resources such as photovoltaic and wind power. However, lithium and cobalt resources are scarce and unevenly distributed across the world,[1,2] which potentially leads to instability in market prices, affected by the political situation of producing countries. Moreover, the utilization of organic solvent-based electrolytes increases the risk of ignition accidents, which are more serious for large-sized batteries.[3]

Under these circumstances, the author focuses on studies involving sodium-ion batteries (Na-ion batteries; NIB) and potassium-ion batteries (K-ion batteries; KIB) with ionic liquid (IL) electrolytes as LIB alternatives. Sodium and potassium resources are abundant in the Earth's crust. Ionic liquids (sometimes called room temperature (or low temperature) molten salts) have safety of negligible volatility and non-flammability; they are composed only of ions, providing unique physicochemical and electrochemical properties. Thus, they have been applied as electrolytes for metal electrodeposition and in various electrochemical devices.[4] In the research field of secondary batteries, inorganic salts have historically been used as electrolytes in molten salt batteries (also known as thermal batteries) typically operating at temperatures higher than

Takayuki Yamamoto (Assistant Professor, Institute of Advanced Energy, Kyoto University)

Takayuki Yamamoto graduated from Graduate School of Energy Science, Kyoto University, and received his Ph.D. degree (Doctor of Energy Science) in March 2016. He worked as JSPS Research Fellowship for Young Scientist (2015–2016), and Researcher in the office of Society Academia Collaboration for Innovation, Kyoto University (2016–2017). He moved to Institute of Advanced Energy, Kyoto University as Assistant Professor in April 2017. His research interests are rechargeable batteries using ionic liquids and various charge carriers.

§ECSJ Active Member
T. Yamamoto (ID) orcid.org/0000-0003-3553-3272

500 K.[5–7] To broaden the range of their application, the electrolytes have been replaced with mixtures of alkali metal amide-based melts such as M[TFSA]s and M[FSA]s (where M = alkali metal, TFSA = bis(trifluoromethylsulfonyl)amide, and FSA = bis(fluorosulfonyl)-amide), which enables battery operation at temperatures of 353–423 K.[8–14] Since the melting points of these mixtures are higher than room temperature, organic cations have been introduced to realize ionic liquid electrolytes for LIBs[15–19] and NIBs[20–24] that function at room temperature. Apart from NIBs and KIBs, novel batteries called beyond-LIBs, which exhibit theoretical energy densities superior to those of current LIBs, have also attracted attention; these include magnesium secondary batteries and metal-air batteries. In the last decade, the number of scientific papers on fluoride-shuttle batteries (FSBs) has gradually increased.[25,26] The principle of FSB operation is very simple, i.e., the naked or solvated fluoride ions shuttle between the positive and negative electrodes, and this confers high energy densities despite the charge carrier being a univalent anion. However, there are significant challenges in the development of electrolytes that enable operation at room temperature. The present paper summarizes the progress achieved by the author and his colleagues on the aforementioned issues, and provides comprehensive insights on next-generation rechargeable batteries utilizing ionic liquids.

2. Sodium-ion Batteries Using Amide-based Ionic Liquid Electrolytes

### 2.1 Electrochemical behavior of tin-based negative electrodes

Tin is a negative electrode material candidate for NIBs owing to its high theoretical capacity ($847 \, \text{mAh} \, (\text{g-Sn})^{-1}$ and $6.17 \, \text{Ah} \, (\text{cm}^3\text{-Sn})^{-1}$). According to the Na–Sn phase diagram,[27] tin forms eight intermetallic compounds with sodium, i.e., $NaSn_6$, $NaSn_4$, $NaSn_3$, $NaSn_2$, α-NaSn, Na_9Sn_4, Na_3Sn, and $Na_{15}Sn_4$, whereas the crystal structures of some of these compounds are unknown. Moreover, other Na–Sn alloy compounds, which are absent in the phase diagram, need to be taken into consideration because their crystal structures have been reported. Thus, Na–Sn system remains the subject of various studies.

First, the electrochemical behavior of tin film on aluminum foil (hereafter, called "tin film electrode") was investigated in Na[FSA]–K[FSA] IL electrolyte at 363 K; this is considered a completely inorganic IL electrolyte, because it does not have organic species. An electrolyte composition of $x(Na[FSA]) = 0.56$ ($x(Na[FSA])$: molar fraction of Na[FSA]) melts at 334 K[12] and shows a moderate ionic conductivity of $3.3 \, \text{mS} \, \text{cm}^{-1}$ at 363 K.[14] The results of cyclic voltammetry (CV) and charge–discharge tests for tin film electrodes suggest reversible alloying and dealloying reactions of tin with sodium. Figure 1 shows the initial charge–discharge curves of a tin film electrode at a current density of $0.619 \, \text{mA} \, \text{cm}^{-2}$ (approximately 0.1 C rate) at 363 K.[28] Only three plateaus appeared in both the charge and discharge processes, indicating the formation of three intermetallic compounds. From the calculated capacities of the Na–Sn alloys and the capacities obtained during the discharge process, the three plateaus were assigned as coexisting states of (a′) α-NaSn/β-Sn, (b′) Na_9Sn_4/α-NaSn, and (c′) $Na_{15}Sn_4$/Na_9Sn_4. The cyclability of each plateau was confirmed by charge–discharge tests using only one plateau, which revealed that plateau (c′) maintained the highest capacity retention ratio after 30 cycles. In general, the cyclability of alloy-based negative electrodes is largely affected by the degree of volume change during the operation. The theoretical volume contraction ratios during discharging were 0.45, 0.63, and 0.66 for plateaus (a′), (b′), and (c′), respectively. Thus, the tentative assignment of the phase transition for the potential plateaus was consistent with the cycling performance.

Since most of the crystalline Na–Sn alloys were obtained by metallurgical processes, X-ray diffraction (XRD) analysis of Na–Sn
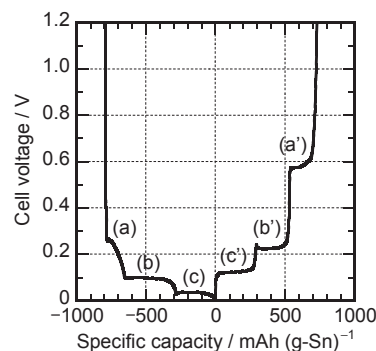

Figure 1. Initial charge–discharge curves of the Na/Na[FSA]–K[FSA]/Sn film cell at 363 K. Cut-off voltages: 0.005 and 1.200 V. Current density: $0.619 \, \text{mA} \, \text{cm}^{-2}$. Reproduced with the permission from Refs. 28 and 29.
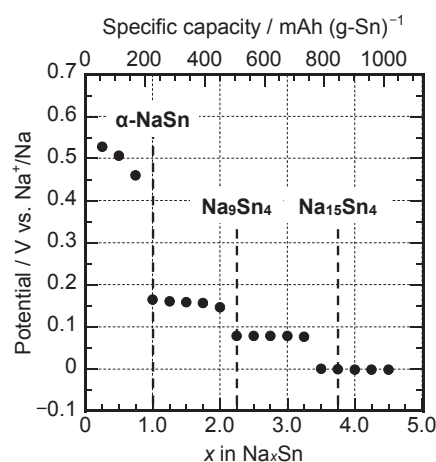
Figure 2. The relation between equilibrium potential and Na composition for Na–Sn alloy determined by GITT using a Na/Na[FSA]–K[FSA]/Sn film cell at 363 K. Reproduced with the permission from Ref. 29.

alloys prepared by electrochemical methods has been used to elucidate the charge–discharge mechanism of the tin negative electrode for NIBs.[29] Figure 2 shows the results of a galvanostatic intermittent titration technique conducted using a Na/Sn two-electrode cell at 363 K in the Na[FSA]–K[FSA] IL electrolyte. Three distinct plateaus were observed at approximately 0.16, 0.08, and 0 V (vs. Na^+/Na). A sloping region was observed in the potential range of 0.45–0.55 V, suggesting multistep reactions for the Na-poor compositions. Then, Na–Sn alloy samples were prepared via a combination of galvanostatic and potentiostatic electrolysis. The tin electrodes at open-circuit potentials of 0.557, 0.225, and 0.007 V conferred the XRD patterns of β-Sn, α-NaSn, and $Na_{15}Sn_4$, respectively. However, the XRD pattern of the sample at 0.122 V did not match any reported patterns obtained from alloys prepared by the metallurgical process. According to reports from another group,[30,31] the $Na_{5-x}Sn_2$ phase belonging to the trigonal R-3m space group is electrochemically formed. Thus, the three plateaus at 0.16, 0.08, and 0 V correspond to the coexisting states of $Na_{5-x}Sn_2$/α-NaSn, $Na_{15}Sn_4$/$Na_{5-x}Sn_2$, and Na/$Na_{15}Sn_4$, respectively. Although further direct investigation proved difficult, the thermodynamic parameters were obtained assuming the existence of the $NaSn_2$ phase, i.e., the equilibrium of $NaSn_2$/β-Sn at 0.53 V and α-NaSn/$NaSn_2$ at 0.46 V. The Gibbs energies of formation were calculated to be −17.0, −23.9, −20.6, and −16.6 kJ (mol-atom)$^{-1}$ for $NaSn_2$, α-
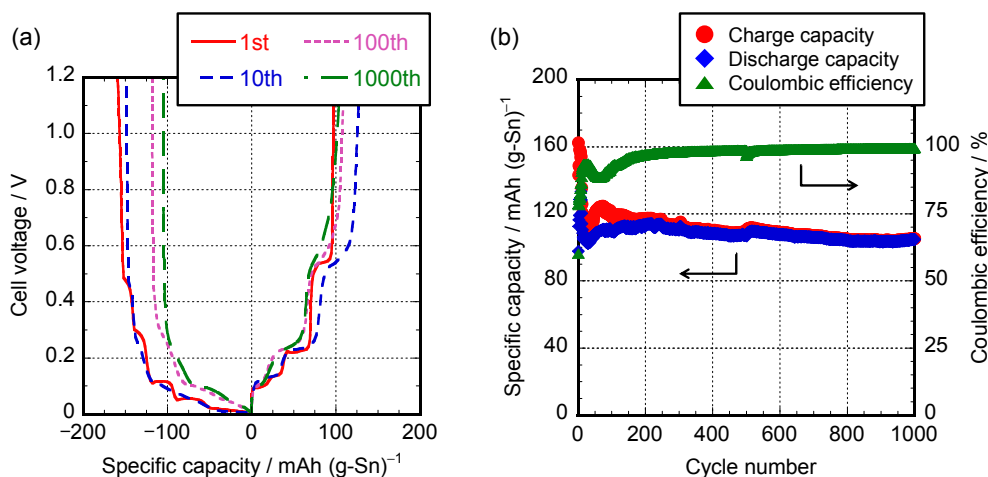
Figure 3. (a) Charge–discharge curves and (b) cycling properties of specific capacity and coulombic efficiency of 4 h-annealed Sn–Cu film at current density of 84.7 mA (g-Sn)$^{-1}$. Reproduced with the permission from Ref. 35.

NaSn, Na$_{5-x}$Sn$_2$ (where x was assumed to be 1/2), and Na$_{15}$Sn$_4$, respectively.

To enhance the cycling properties of alloy-based negative electrodes, the introduction of buffer materials is effective because the structural deformation of the electrodes is suppressed by mitigating the strain generated by large volume changes during operation. The volume of active material increases by 5.3 times when Na$_{15}$Sn$_4$ is formed from β-Sn, which is much larger than in the case of the Li–graphite system (1.1 times volume change).[32] Thus, TM–Sn alloys (where TM = Cu, Ni, Fe) were prepared by the annealing of tin film (approximately 1 μm thickness) onto TM current collectors (hereafter, called "Sn–TM films"), which was inspired by previous studies on tin negative electrodes for LIBs.[33,34]

In a study on Sn–Cu films,[35] a non-annealed film composed of β-Sn and Cu$_6$Sn$_5$ phases was investigated. After 10 h of annealing at 463 K, β-Sn disappeared and the Cu$_6$Sn$_5$ and Cu$_3$Sn regions increased. The reversible capacities decreased with annealing time, whereas the capacity retention ratios were improved. Figure 3 shows the charge–discharge profiles and cycling properties of a Sn–Cu film annealed for 4 h at 463 K. Discharge capacities of 100–120 mAh (g-Sn)$^{-1}$ were maintained for 1000 cycles, indicating appropriate stability for long-term operation. Most of the reversible capacities were derived from the β-Sn phase; however, Cu$_6$Sn$_5$ was also found to act as an active material based on the ex-situ XRD results. In contrast, Cu$_3$Sn was inactive with sodium.

Similar studies have been conducted on Sn–Ni and Sn–Fe films.[36,37] Metastable needle-like NiSn$_3$ and stable laminar Ni$_3$Sn$_4$ phases were observed in the non-annealed Sn–Ni film. In contrast to the Sn–Cu films, the reversible capacities quickly decreased within 10 cycles after annealing at 463 K for 2 and 10 h. According to cross-sectional field emission-scanning electron microscopy (FE-SEM), the rapid capacity decline was caused by the collapse of the thick Ni$_3$Sn$_4$ layer between the β-Sn layer and the Ni current collector. Ni$_3$Sn$_4$ was found to be inactive with sodium, which differs from the situation with LIBs.[38,39] In the case of the Sn–Fe films, annealed films were prepared at 533 K over 0–45 h. An intermetallic compound, FeSn$_2$, appeared after the annealing process and was slightly active with sodium. Although the annealed films showed better cyclability than the non-annealed film, their reversible capacities were less than 100 mAh (g-Sn)$^{-1}$.

2.2 Improved performance of full-cells with highly concentrated electrolytes

Several room temperature ionic liquids (RTILs) have been investigated as possible NIB electrolytes.[20–24,40,41] Among them, pyrrolidinium-based RTILs are promising because of their relatively high ionic conductivities and electrochemical stabilities. The Na[FSA]–[C$_3$C$_1$pyrr][FSA] (C$_3$C$_1$pyrr = *N*-methyl-*N*-propylpyrrolidinium) IL exists as a liquid phase at room temperature (298 K) within a compositional range of x(Na[FSA]) = 0–0.50. The composition of x(Na[FSA]) = 0.20 exhibited moderate ionic conductivities of 3.6 and 10.6 mS cm^{-1} at 298 and 333 K, respectively.

The charge–discharge behaviors of several positive and negative electrodes have been investigated in this IL using half-cells with a Na metal counter electrode.[42–44] Full-cell performance was also evaluated, which proved that both coin-type and large-sized hard carbon (HC)/NaCrO$_2$ cells exhibited practical performance.[45] However, the full-cell capacity rapidly decreased at higher current rates and the degradation mechanism was unclarified. A simple strategy to improve the rate capability is to increase the concentration of charge carrier, i.e. Na$^+$ ion in the electrolyte. The enhancement of rate capability was previously reported for several positive electrodes using Na$^+$ ion-concentrated IL electrolytes,[46,47] despite the Na$^+$ ionic conductivities decrease with increasing Na$^+$ ion concentration in the bulk electrolyte.[48] Thus, the author and his colleagues investigated the charge–discharge mechanism of NIBs with highly concentrated IL electrolytes at 333 K using three-electrode HC/NaCrO$_2$ full-cells with a Na metal reference electrode.[49]

Figure 4a shows the charge–discharge curves of the HC/NaCrO$_2$ full-cell using the Na[FSA]–[C$_3$C$_1$pyrr][FSA] IL electrolyte at a composition of x(Na[FSA]) = 0.20 at a charge–discharge rate of 0.5 C (1 C = 100 mA (g-NaCrO$_2$)$^{-1}$). The charge–discharge profiles of HC and NaCrO$_2$ were clearly separated, enabling the evaluation of the rate-determining process in the full-cell. A reversible capacity of 91.5 mAh (g-NaCrO$_2$)$^{-1}$ was obtained at an average operating potential of 2.72 V, resulting in a gravimetric energy density of 177 Wh (kg-(NaCrO$_2$ + HC))$^{-1}$. Figures 4b and 4c show the discharge curves of the full-cells at various discharge rates using Na[FSA]–[C$_3$C$_1$pyrr][FSA] IL electrolytes at compositions of x(Na[FSA]) = 0.20 and 0.40, respectively. The HC/NaCrO$_2$ full-cell using an electrolyte with a lower Na composition rapidly degraded at discharge rates higher than 2 C. In contrast, the highly concentrated electrolytes delivered superior capacity retention ratios, even at 2 C. By comparing the discharge curves at a 2 C rate for both electrolytes, a clear difference can be seen in the profiles of the NaCrO$_2$ positive electrode. The positive electrode potential suddenly dropped at a capacity of approximately 50 mAh (g-NaCrO$_2$)$^{-1}$ in the

(a) x(Na[FSA]) = 0.20

(b) x(Na[FSA]) = 0.20

(c) x(Na[FSA]) = 0.40
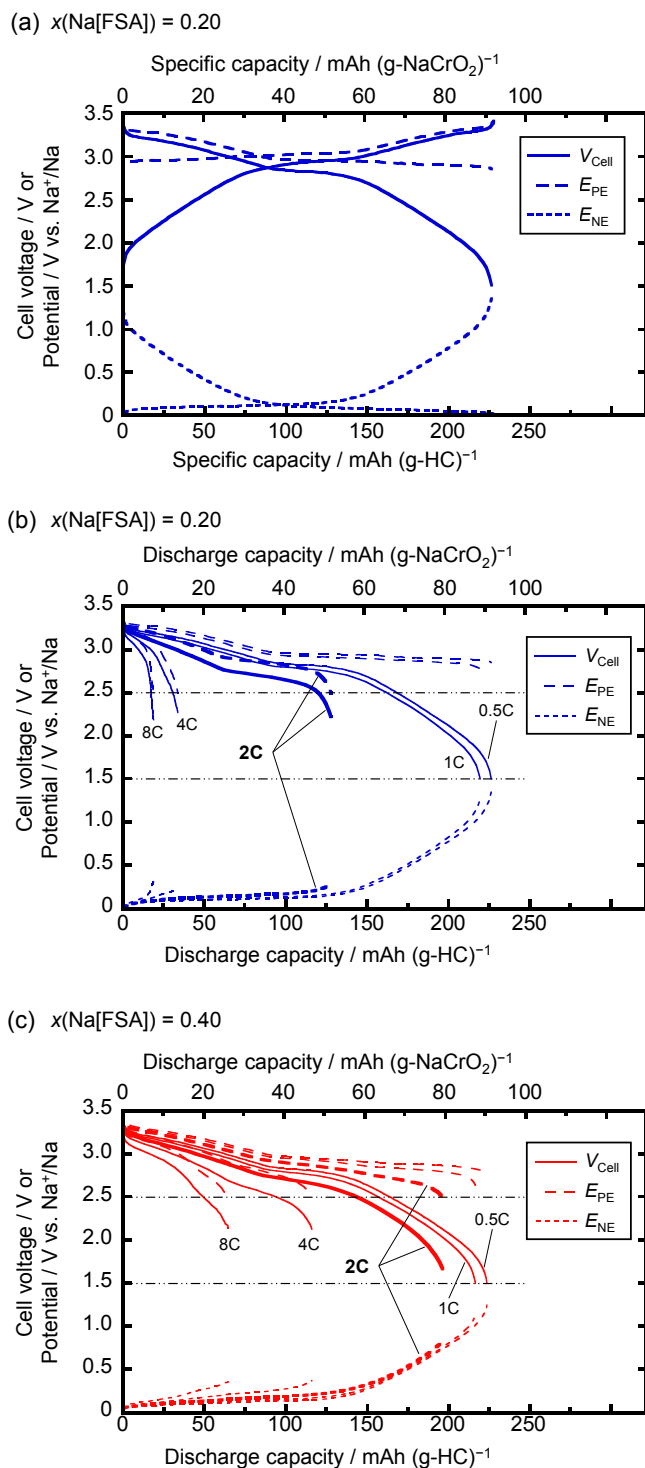
Figure 4. (a) Charge–discharge curves of a HC/Na[FSA]–[C$_3$C$_1$pyrr][FSA]/NaCrO$_2$ full-cell (x(Na[FSA]) = 0.20). Operating temperature: 333 K. Charge–discharge rate: 0.5 C (1 C = 100 mA (g-NaCrO$_2$)$^{-1}$). The legends, V_{Cell}, E_{PE}, and E_{NE} are the cell voltage, the potential of the NaCrO$_2$ positive electrode and the potential of the HC negative electrode, respectively. (b and c) Discharge curves of the HC/Na[FSA]–[C$_3$C$_1$pyrr][FSA]/NaCrO$_2$ full-cells at 333 K. Charge rate: 0.5 C. Discharge rates: 0.5–8 C (1 C = 100 mA (g-NaCrO$_2$)$^{-1}$). The electrolyte compositions: (b) x(Na[FSA]) = 0.20 and (c) x(Na[FSA]) = 0.40. Reproduced with the permission from Ref. 49.

case of the electrolyte with x(Na[FSA]) = 0.20, suggesting an increase in the reaction resistance during the discharge process. Since a similar behavior was observed in the HC negative electrode
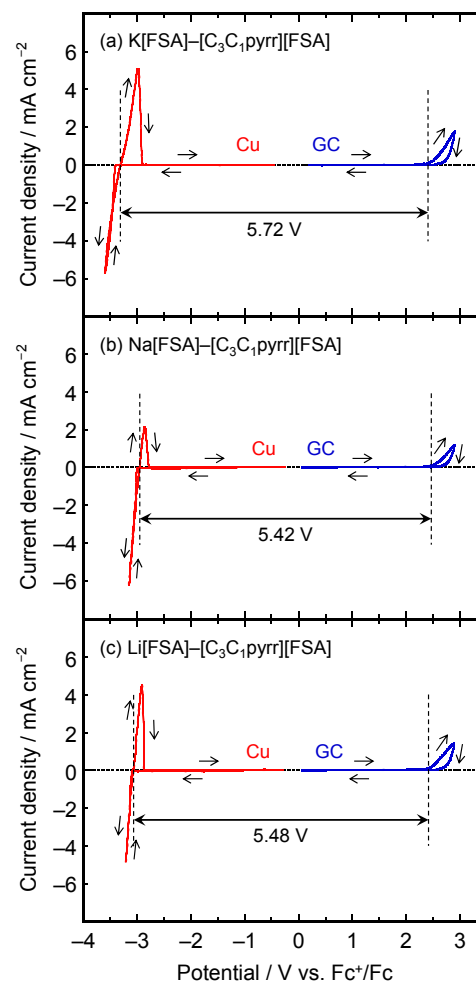
Figure 5. Cyclic voltammograms of (a) K[FSA]–[C$_3$C$_1$pyrr][FSA] (x(K[FSA]) = 0.20), (b) Na[FSA]–[C$_3$C$_1$pyrr][FSA] (x(Na[FSA]) = 0.20), (c) Li[FSA]–[C$_3$C$_1$pyrr][FSA] (x(Li[FSA]) = 0.20) at 298 K. Working electrodes: copper disk (cathode limit) and glassy carbon disk (anodic limit). Scan rate: 5 mV s^{-1}. Cycle number: 1st. Cathode and anode limits of each electrolyte are indicated by dashed lines. Reproduced with the permission from Ref. 55. Copyright 2017 American Chemical Society

for the charge rate capability test, the Na$^+$ ion intercalation process is likely to be the rate-determining step of the full-cell, which indicates that the depletion of Na$^+$ ions occurs in the electrolyte in the vicinity of the NaCrO$_2$ electrode surface during the discharging step. Further investigation is required to elucidate these phenomena.

3. Potassium-ion Chemistry in Ionic Liquids

3.1 Development of ionic liquid electrolytes

Potassium-ion batteries (KIBs) are promising because of the abundance of potassium resources and their high operating voltages. After the publication of pioneering works on KIBs,[50–52] the number of scientific papers has rapidly increased in recent decades.[53,54] The author has focused on the possibility of KIBs utilizing IL electrolytes[55–61] because the electrode potential of potassium is empirically known to be more negative than that of lithium in many molten salts and ionic liquids. K[FSA]–[C$_3$C$_1$pyrr][FSA] IL was selected as a KIB electrolyte candidate, and its physicochemical and electrochemical properties were systematically compared to those of its lithium and sodium counterparts.[55] Figure 5 shows cyclic voltammograms of M[FSA]–[C$_3$C$_1$pyrr][FSA] (M = Li, Na, K;
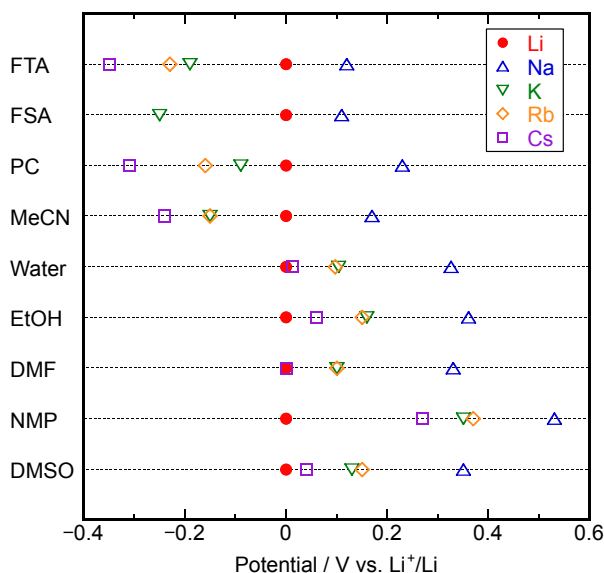
Figure 6. Redox potentials of alkali metals ($E(M^+/M)$; M = alkali metal) in various electrolytes with respect to $E(Li^+/Li)$. FTA = M[FTA]–[C$_4$C$_1$pyrr][FTA] ($C(Li^+) = 0.820 \, \mathrm{mol \, dm^{-3}}$, $C(Na^+) = 0.819 \, \mathrm{mol \, dm^{-3}}$, $C(K^+) = 0.814 \, \mathrm{mol \, dm^{-3}}$, $C(Rb^+) = 0.811 \, \mathrm{mol \, dm^{-3}}$, $C(Cs^+) = 0.806 \, \mathrm{mol \, dm^{-3}}$), FSA = M[FSA]–[C$_3C_1$pyrr][FSA] ($C(Li^+) = 1.0 \, \mathrm{mol \, dm^{-3}}$, $C(Na^+) = 0.98$ mol dm^{-3}, $C(K^+) = 0.98 \, \mathrm{mol \, dm^{-3}}$), PC = propylene carbonate ($C(M^+) = 1 \, \mathrm{mol \, dm^{-3}}$), MeCN = acetonitrile ($C(M^+) = 1 \, \mathrm{mol \, dm^{-3}}$), EtOH = ethanol ($C(M^+) = 1 \, \mathrm{mol \, dm^{-3}}$), DMF = *N,N*-dimethylformamide ($C(M^+) = 1 \, \mathrm{mol \, dm^{-3}}$), NMP = *N*-methyl-pyrrolidone ($C(M^+) = 1 \, \mathrm{mol \, dm^{-3}}$), DMSO = dimethyl sulfoxide ($C(M^+) = 1 \, \mathrm{mol \, dm^{-3}}$). Reproduced with the permission from Ref. 59. Copyright 2020 American Chemical Society

$x(M[FSA]) = 0.20$) obtained at 298 K. The redox potentials of alkali metals (V vs. Fc$^+$/Fc; Fc = ferrocene) are −3.07 V (Li), −2.96 V (Na), and −3.31 V (K). Since the oxidative limit potentials, which are ascribed to FSA$^-$ decomposition, are almost the same among these systems, the K-ion system possesses the widest electrochemical window of 5.72 V, leading to the possibility of electrolyte for high-voltage KIBs. K[FSA]–[C$_3$C$_1$pyrr][FSA] IL at a composition of $x(K[FSA]) = 0.20$ exhibited a reasonably high ionic conductivity of 4.8 mS cm^{-1} at 298 K, which was higher than that of its sodium counterpart (3.6 mS cm^{-1} at 298 K).[48] Therefore, this IL has been adopted as the standard electrolyte for KIBs. The battery performance results are discussed in the next section. Similar trends in the electrolyte properties were also confirmed for M[FSA]–[C$_2$C$_1$im][FSA] (C$_2$C$_1$im = 1-ethyl-3-methylimidazolium) ILs.[60] The redox potentials of alkali metals were further investigated using the M[FTA]–[C$_4$C$_1$pyrr][FTA] system (M = Li, Na, K, Rb, Cs; FTA = (fluorosulfonyl)(trifluoromethylsulfonyl)amide; C$_4$C$_1$pyrr = *N*-butyl-*N*-methylpyrrolidinium).[59] The redox potentials increased in the following order: Cs < Rb < K < Li < Na. Figure 6 summarizes the redox potentials of the alkali metals ($E(M^+/M)$) with respect to the Li$^+$/Li potential in various electrolytes. Except for the ionic liquids, the redox potentials were obtained via thermodynamic calculations (not by electrochemical measurements).[62] The trend of the redox potentials is classified into two types: $E(Li^+/Li)$ is the most negative in water and many organic solvents, and $E(Cs^+/Cs)$ is the most negative in ionic liquids and some organic solvents such as propylene carbonate and acetonitrile.

3.2 Performance evaluation of potassium-ion batteries

To ascertain the feasibility of KIBs, charge–discharge perform-

ances of several active materials have been evaluated using the K[FSA]–[C$_3$C$_1$pyrr][FSA] IL electrolyte. First, tin was selected as a representative alloy-based negative electrode material, which gave theoretical capacities of 452 and 226 mAh (g-Sn)$^{-1}$ for the formation of K$_2$Sn and KSn, respectively. However, the reversible capacities were approximately 200 mAh (g-Sn)$^{-1}$ in previous reports using organic solvent-based electrolytes, suggesting the formation of a KSn phase. The authors investigated the charge–discharge mechanism of tin negative electrode materials composed of submicron tin powder, acetylene black (AB) as a conductive agent, and polyamide–imide (PAI) binder using the K[FSA]–[C$_3$C$_1$pyrr][FSA] IL electrolyte at 298 K.[57] An initial discharge capacity of 186 mAh (g-Sn)$^{-1}$ was obtained at 20 mA (g-Sn)$^{-1}$, which is comparable to that reported in other studies. The formation of the KSn phase in the fully charged state was confirmed by ex-situ XRD, commensurate with the obtained capacities. The reversible capacity of 173 mAh (g-Sn)$^{-1}$ was retained even after 100 cycles, which was the highest capacity retention reported among the previous studies on tin negative electrodes for KIBs. This might be originated from the superior reductive stability of IL electrolytes compared to that of organic solvents.

Recently, we reported the charge–discharge behavior of graphite negative electrodes using the same IL electrolyte.[61] The phase evolution behavior of the graphite composite electrodes with sodium carboxylmethyl cellulose (CMC) binder was comprehensively analyzed by ex-situ XRD, revealing the formation of stage-1 KC$_8$, stage-2 KC$_{24}$, and stage-3 KC$_{36}$ in both the charging and discharging processes. In addition, a hysteresis of potential profiles exists in the high-stage regions (K-poor compositions), as confirmed by XRD and galvanostatic intermittent titration technique (GITT). The graphite electrodes exhibited stable cycling properties for over 200 cycles, retaining a reversible capacity of 200 mAh (g-C)$^{-1}$. From an academic viewpoint, it is interesting to compare the formation capability of graphite intercalation compounds (GICs) in alkali metal-ion systems, because Li and K can form stage-1 GICs, whereas Na cannot. Figure 7 shows the initial charge–discharge curves at 298 K, which were obtained using three-electrode cells with alkali metal reference electrodes and converted to the Fc$^+$/Fc potentials according to a previous study.[55] It was found that the binary alkali metal GICs were preferably formed at potentials below −2.85 V vs. Fc$^+$/Fc, which is very close to the Na$^+$/Na potential (−2.96 V), probably leading to the difficulty of the formation of low-stage Na-GICs.
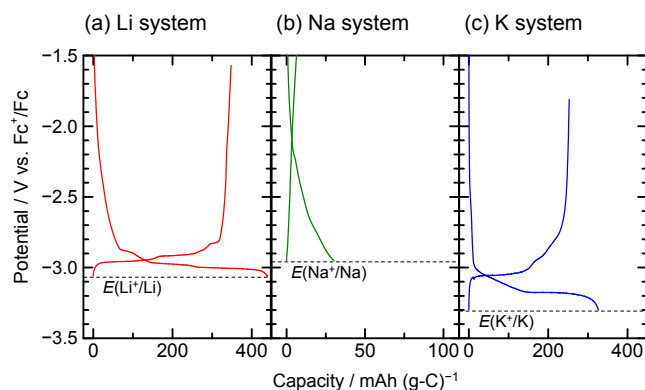
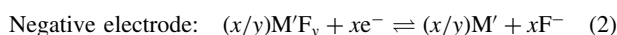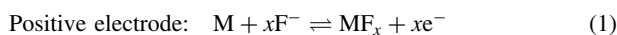**Figure 7.** Initial charge–discharge curves for M/graphite cell (M = Li, Na, K) using M[FSA]–[C$_3$C$_1$pyrr][FSA] ($x(M[FSA]) = 0.20$, M = Li, Na, K) electrolyte at 298 K using three-electrode cell configuration. Current rates: 37.2, 1.5, and 27.9 mA g^{-1} for Li-, Na-, and K-ion system, respectively. Reproduced with the permission from Ref. 61.
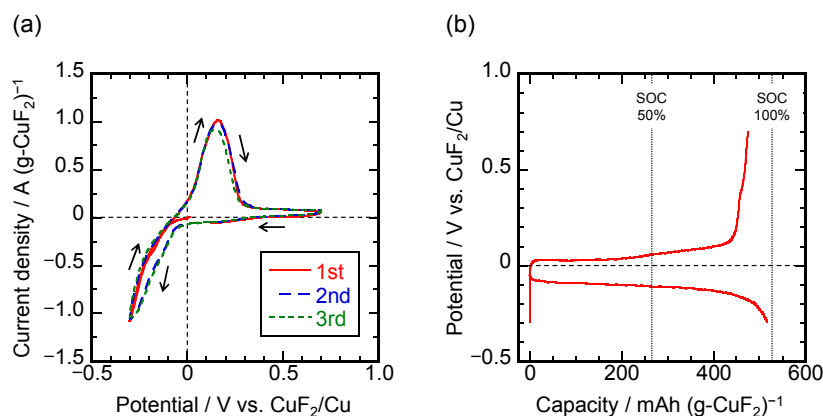
Figure 8. (a) Cyclic voltammograms and (b) subsequent charge–discharge curve of CuF$_2$ electrode in [C$_2$C$_1$im][(FH)$_{2.3}$F] at 298 K. Scan rate: 10 mV s^{-1}; charge–discharge rate: 0.05 C (= 26.4 mA (g-CuF$_2$)$^{-1}$). The term, SOC (= state of charge), corresponds to the proportion of the capacity to the theoretical capacity. Reproduced with the permission from Ref. [77]. Copyright 2013 American Chemical Society

4. Fluoride-shuttle Batteries Using Fluorohydrogenate Ionic Liquids

Fluoride-shuttle batteries (FSBs) are among the most attractive candidates for next-generation batteries. Metals (M or M′) or their fluorides (MF$_x$ or M′F$_y$) are used in most FSB studies and usually induce multielectron reactions according to the following equations:

Positive electrode: $\quad M + xF^- \rightleftharpoons MF_x + xe^-$ $\quad$ (1)

Negative electrode: $\quad (x/y)M'F_y + xe^- \rightleftharpoons (x/y)M' + xF^-$ $\quad$ (2)

Historically, inorganic solid-state electrolytes with fluoride ion conductivities have been investigated,[63–65] which led to an epoch-making study that fluoride ions reversibly shuttle between positive and negative electrodes.[66] Many scientific papers have been published on this subject in the past decade;[25,26] however, sufficient performance has only been achieved at temperatures higher than 373 K. Conversely, several novel electrolytes that are operable at room temperature have been proposed, for example, organic solvents[67–70] and ionic liquids.[71,72] Ether-based organic electrolytes containing CsF and anion acceptors exhibit reversible fluorination/defluorination behavior with BiF$_3$ and PbF$_2$ positive electrodes.[67,69,70] New organic fluoride salts with high solubility in organic solvents have been reported, enabling battery applications for various active materials.[68]

Based on this background, the author and his colleagues have focused on fluorohydrogenate ionic liquids (FHILs) as FSB electrolytes. FHILs are composed of organic/metal cations and fluorohydrogenate anions, [(FH)$_n$F]$^-$ (n = HF composition),[73] and show extremely high ionic conductivities as non-aqueous electrolytes owing to the weak ionic interactions derived from fast HF exchange between [(FH)$_n$F]$^-$ anions.[74] A representative FHIL, [C$_2$C$_1$im][(FH)$_{2.3}$F], exhibited an ionic conductivity of 100 mS cm^{-1} at 298 K,[75] which is much higher than that of ILs containing the [C$_2$C$_1$im]$^+$ cation.[76] Copper-based materials have subsequently been selected as the positive electrode materials because of their high theoretical capacities of 528 mAh (g-CuF$_2$)$^{-1}$ and 844 mAh (g-Cu)$^{-1}$. Figure [8] represents cyclic voltammograms and subsequent charge–discharge curve of a CuF$_2$ composite electrode with the AB conductive agent and PTFE binder in a [C$_2$C$_1$im][(FH)$_{2.3}$F] electrolyte at 298 K.[77] The obtained discharge and charge capacities were 517 and 475 mAh (g-CuF$_2$)$^{-1}$, which are commensurate with 98 and 90% of the theoretical capacity, respectively, and are the highest capacities ever reported. Figure [9] summarizes the results of X-ray photoelectron spectroscopy (XPS) obtained at selected charge–discharge states. Broad peaks assignable to CuF$_2$ observed
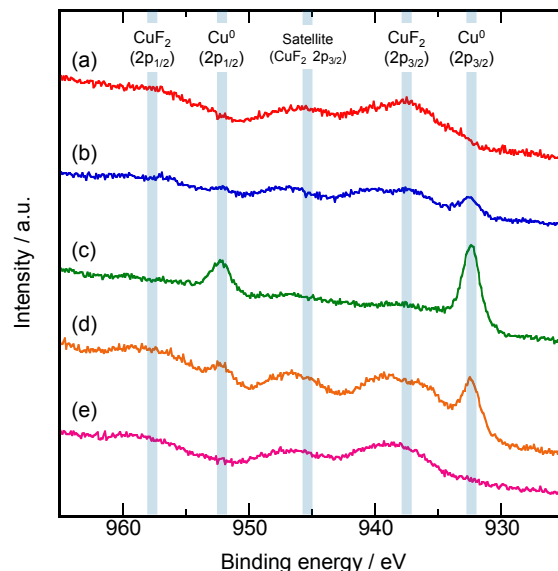
Figure 9. XPS profiles of CuF$_2$ electrodes at various charge–discharge states. (a) Pristine, (b) after discharging to 50% of the theoretical capacity (264 mAh (g-CuF$_2$)$^{-1}$), (c) after discharging to -0.3 V vs. CuF$_2$/Cu, (d) after charging to 50% of the theoretical capacity (264 mAh (g-CuF$_2$)$^{-1}$), and (e) after charging to 0.7 V vs. CuF$_2$/Cu in [C$_2$C$_1$im][(FH)$_{2.3}$F] at 298 K. Reproduced with the permission from Ref. [77]. Copyright 2013 American Chemical Society

in the pristine electrodes continuously decreased during the initial charging process, whereas sharper peaks derived from metallic copper appeared and became stronger. Following subsequent charging processes, the CuF$_2$ peaks, which almost vanished in the fully charged state, recovered to the original state. Since the reformed CuF$_2$ could not be detected by XRD, it was obviously amorphous.

The high reversible capacities can be explained by dissolution and precipitation mechanisms. According to inductively coupled plasma-atomic emission spectroscopy (ICP-AES), CuF$_2$ is dissolved in [C$_2$C$_1$im][(FH)$_{2.3}$F] at up to 100 ppm (= 100 (mg-Cu) dm^{-3}). Thus, under pristine conditions, CuF$_2$ exists in equilibrium with the chemically dissolved copper species (e.g., [CuF$_4$]$^{2-}$) in the electrolyte. When the electrochemical fluorination of copper occurs during the charge process, the copper is first dissolved into the electrolyte to

form ionic species, and then precipitates on the electrode surface as CuF_2. This indirect formation is a possible reason for the low crystallinity of the reformed CuF_2. Similar studies were conducted using metallic copper in the initial state because practical batteries should be constructed in discharged states owing to their chemical stability. In addition to $[C_2C_1im][(FH)_{2.3}F]$, another FHIL, $[C_2C_1pyrr][(FH)_{2.3}F]$ ($C_2C_1pyrr = N$-ethyl-N-methylpyrrolidinium), which possesses a relatively high ionic conductivity of $74.6\,mS\,cm^{-1}$ at $298\,K$, has been applied as an FSB electrolyte.[78] The copper metal composite electrodes exhibited a better capacity retention ratio for the $[C_2C_1pyrr][(FH)_{2.3}F]$ electrolyte, due to CuF_2 solubility being as low as 20 ppm in this FHIL.[79] Combined with the results of surface scanning electron microscopy–energy dispersive X-ray analysis (SEM–EDX) mapping, it was found that the low solubility suppressed the migration of copper species, preventing aggregation of the active materials. Therefore, controlling the solubility of the active materials is a key factor in the construction of FSBs with longer cyclability.

5. Conclusions

This comprehensive paper introduced representative results of studies on next-generation batteries that utilize ionic liquid electrolytes. The study of tin negative electrodes for NIBs elucidated their fundamental electrochemical behaviors and strategies for improved cyclability. The origin of the superior battery performance using highly concentrated electrolytes was analyzed in detail using three-electrode NIB full-cells; however, there is still scope for future examination. Several IL electrolytes for KIBs have been developed and applied to the evaluation of various negative electrode materials. A comparison of the electrolyte properties of alkali metal-ion systems has revealed some interesting findings from an academic viewpoint. FHIL electrolytes conferred the full utilization of CuF_2 positive electrodes for FSBs owing to specific dissolution and precipitation mechanisms. The application of IL electrolytes broadens the possibilities for the development of safe and high-performance novel electrochemical devices.

CRediT Authorship Contribution Statement

Takayuki Yamamoto: Conceptualization (Lead), Investigation (Lead), Writing – original draft (Lead), Writing – review & editing (Lead)

Conflict of Interest

The authors declare no conflict of interest in the manuscript.

References

1. U.S. Geological Survey, Mineral Commodity Summaries 2022, https://pubs.usgs.gov/periodicals/mcs2022/mcs2022.pdf (2022).
2. D. Larcher and J. M. Tarascon, *Nat. Chem.*, **7**, 19 (2015).
3. Q. Wang, B. Mao, S. I. Stoliarov, and J. Sun, *Prog. Energy Combust. Sci.*, **73**, 95 (2019).
4. M. Watanabe, M. L. Thomas, S. Zhang, K. Ueno, T. Yasuda, and K. Dokko, *Chem. Rev.*, **117**, 7190 (2017).
5. D. R. Vissers, Z. Tomczuk, and R. K. Steunenberg, *J. Electrochem. Soc.*, **121**, 665 (1974).
6. E. C. Gay, D. R. Vissers, F. J. Martino, and K. E. Anderson, *J. Electrochem. Soc.*, **123**, 1591 (1976).
7. T. Kasajima, T. Nishikiori, T. Nohira, and Y. Ito, *Electrochem. Solid-State Lett.*, **6**, A109 (2003).
8. R. Hagiwara, K. Tamaki, K. Kubota, T. Goto, and T. Nohira, *J. Chem. Eng. Data*, **53**, 355 (2008).
9. K. Kubota, K. Tamaki, T. Nohira, T. Goto, and R. Hagiwara, *Electrochim. Acta*, **55**, 1113 (2010).
10. A. Watarai, K. Kubota, M. Yamagata, T. Goto, T. Nohira, R. Hagiwara, K. Ui, and N. Kumagai, *J. Power Sources*, **183**, 724 (2008).
11. K. Kubota, T. Nohira, T. Goto, and R. Hagiwara, *Electrochem. Commun.*, **10**, 1886 (2008).
12. K. Kubota, T. Nohira, and R. Hagiwara, *J. Chem. Eng. Data*, **55**, 3142 (2010).
13. T. Nohira, T. Ishibashi, and R. Hagiwara, *J. Power Sources*, **205**, 506 (2012).
14. A. Fukunaga, T. Nohira, Y. Kozawa, R. Hagiwara, S. Sakai, K. Nitta, and S. Inazawa, *J. Power Sources*, **209**, 52 (2012).
15. H. Sakaebe and H. Matsumoto, *Electrochem. Commun.*, **5**, 594 (2003).
16. B. Garcia, S. Lavallée, G. Perron, C. Michot, and M. Armand, *Electrochim. Acta*, **49**, 4583 (2004).
17. H. Matsumoto, H. Sakaebe, K. Tatsumi, M. Kikuta, E. Ishiko, and M. Kono, *J. Power Sources*, **160**, 1308 (2006).
18. M. Ishikawa, T. Sugimoto, M. Kikuta, E. Ishiko, and M. Kono, *J. Power Sources*, **162**, 658 (2006).
19. A. Guerfi, S. Duchesne, Y. Kobayashi, A. Vijh, and K. Zaghib, *J. Power Sources*, **175**, 866 (2008).
20. L. S. Plashnitsa, E. Kobayashi, Y. Noguchi, S. Okada, and J. Yamaki, *J. Electrochem. Soc.*, **157**, A536 (2010).
21. S. A. Mohd Noor, P. C. Howlett, D. R. MacFarlane, and M. Forsyth, *Electrochim. Acta*, **114**, 766 (2013).
22. C. Ding, T. Nohira, K. Kuroda, R. Hagiwara, A. Fukunaga, S. Sakai, K. Nitta, and S. Inazawa, *J. Power Sources*, **238**, 296 (2013).
23. D. Monti, E. Jónsson, M. R. Palacín, and P. Johansson, *J. Power Sources*, **245**, 630 (2014).
24. L. G. Chagas, D. Buchholz, L. Wu, B. Vortmann, and S. Passerini, *J. Power Sources*, **247**, 377 (2014).
25. F. Gschwind, G. Rodriguez-Garcia, D. J. S. Sandbeck, A. Gross, M. Weil, M. Fichtner, and N. Hörmann, *J. Fluorine Chem.*, **182**, 76 (2016).
26. G. Karkera, M. A. Reddy, and M. Fichtner, *J. Power Sources*, **481**, 228877 (2021).
27. T. B. Massalski, *Binary Alloy Phase Diagrams* (2nd ed.), ASM International, Ohio (1990).
28. T. Yamamoto, T. Nohira, R. Hagiwara, A. Fukunaga, S. Sakai, K. Nitta, and S. Inazawa, *J. Power Sources*, **217**, 479 (2012).
29. T. Yamamoto, T. Nohira, R. Hagiwara, A. Fukunaga, S. Sakai, K. Nitta, and S. Inazawa, *J. Power Sources*, **237**, 98 (2013).
30. L. Baggetto, P. Ganesh, R. P. Meisner, R. R. Unocic, J.-C. Jumas, C. A. Bridges, and G. M. Veith, *J. Power Sources*, **234**, 48 (2013).
31. L. Baggetto, C. A. Bridges, J.-C. Jumas, D. R. Mullins, K. J. Carroll, R. A. Meisner, E. J. Crumlin, X. Liu, W. Yang, and G. M. Veith, *J. Mater. Chem. A*, **2**, 18959 (2014).
32. T. Ohzuku, Y. Iwakoshi, and K. Sawai, *J. Electrochem. Soc.*, **140**, 2490 (1993).
33. N. Tamura, R. Ohshita, M. Fujimoto, S. Fujitani, M. Kamino, and I. Yonezu, *J. Power Sources*, **107**, 48 (2002).
34. N. Tamura, R. Ohshita, M. Fujimoto, M. Kamino, and S. Fujitani, *J. Electrochem. Soc.*, **150**, A679 (2003).
35. T. Yamamoto, T. Nohira, R. Hagiwara, A. Fukunaga, S. Sakai, K. Nitta, and S. Inazawa, *Electrochim. Acta*, **135**, 60 (2014).
36. T. Yamamoto, T. Nohira, R. Hagiwara, A. Fukunaga, S. Sakai, and K. Nitta, *Electrochim. Acta*, **193**, 275 (2016).

37. T. Yamamoto, T. Nohira, R. Hagiwara, A. Fukunaga, S. Sakai, and K. Nitta, *Electrochim. Acta*, **211**, 234 (2016).

38. H. Mukaibo, T. Sumi, T. Yokoshima, T. Momma, and T. Osaka, *Electrochem. Solid-State Lett.*, **6**, A218 (2003).

39. J. Hassoun, S. Panero, and B. Scrosati, *J. Power Sources*, **160**, 1336 (2006).

40. K. Matsumoto, T. Hosokawa, T. Nohira, R. Hagiwara, A. Fukunaga, K. Numata, E. Itani, S. Sakai, K. Nitta, and S. Inazawa, *J. Power Sources*, **265**, 36 (2014).

41. K. Matsumoto, R. Taniki, T. Nohira, and R. Hagiwara, *J. Electrochem. Soc.*, **162**, A1409 (2015).

42. C.-Y. Chen, K. Matsumoto, T. Nohira, C. Ding, T. Yamamoto, and R. Hagiwara, *Electrochim. Acta*, **133**, 583 (2014).

43. H. Usui, Y. Domi, K. Fujiwara, M. Shimizu, T. Yamamoto, T. Nohira, R. Hagiwara, and H. Sakaguchi, *ACS Energy Lett.*, **2**, 1139 (2017).

44. T. Yamamoto, T. Yamaguchi, T. Nohira, R. Hagiwara, A. Fukunaga, S. Sakai, and K. Nitta, *Electrochemistry*, **85**, 391 (2017).

45. A. Fukunaga, T. Nohira, R. Hagiwara, K. Numata, E. Itani, S. Sakai, and K. Nitta, *J. Appl. Electrochem.*, **46**, 487 (2016).

46. C. Ding, T. Nohira, R. Hagiwara, K. Matsumoto, Y. Okamoto, A. Fukunaga, S. Sakai, K. Nitta, and S. Inazawa, *J. Power Sources*, **269**, 124 (2014).

47. C.-Y. Chen, T. Kiko, T. Hosokawa, K. Matsumoto, T. Nohira, and R. Hagiwara, *J. Power Sources*, **332**, 51 (2016).

48. K. Matsumoto, Y. Okamoto, T. Nohira, and R. Hagiwara, *J. Phys. Chem. C*, **119**, 7648 (2015).

49. T. Yamamoto, K. Mitsuhashi, K. Matsumoto, R. Hagiwara, A. Fukunaga, S. Sakai, K. Nitta, and T. Nohira, *Electrochemistry*, **87**, 175 (2019).

50. A. Eftekhari, *J. Power Sources*, **126**, 221 (2004).

51. N. Recham, G. Rousse, M. T. Sougrati, J.-N. Chotard, C. Frayret, S. Mariyappan, B. C. Melot, J.-C. Jumas, and J.-M. Tarascon, *Chem. Mater.*, **24**, 4363 (2012).

52. S. Komaba, T. Hasegawa, M. Dahbi, and K. Kubota, *Electrochem. Commun.*, **60**, 172 (2015).

53. A. Eftekhari, Z. Jian, and X. Ji, *ACS Appl. Mater. Interfaces*, **9**, 4404 (2017).

54. T. Hosaka, K. Kubota, A. S. Hameed, and S. Komaba, *Chem. Rev.*, **120**, 6358 (2020).

55. T. Yamamoto, K. Matsumoto, R. Hagiwara, and T. Nohira, *J. Phys. Chem. C*, **121**, 18450 (2017).

56. Y. Domi, H. Usui, E. Nakabayashi, T. Yamamoto, T. Nohira, and H. Sakaguchi, *Electrochemistry*, **87**, 333 (2019).

57. T. Yamamoto and T. Nohira, *Chem. Commun.*, **56**, 2538 (2020).

58. H. Onuma, K. Kubota, S. Muratsubaki, T. Hosaka, R. Tatara, T. Yamamoto, K. Matsumoto, T. Nohira, R. Hagiwara, H. Oji, S. Yasuno, and S. Komaba, *ACS Energy Lett.*, **5**, 2849 (2020).

59. T. Yamamoto, S. Nishijima, and T. Nohira, *J. Phys. Chem. B*, **124**, 8380 (2020).

60. T. Yamamoto, R. Matsubara, and T. Nohira, *J. Chem. Eng. Data*, **66**, 1081 (2021).

61. T. Yamamoto, A. Yadav, and T. Nohira, *J. Electrochem. Soc.*, **169**, 050507 (2022).

62. Y. Marcus, *Pure Appl. Chem.*, **57**, 1129 (1985).

63. J. H. Kennedy, R. Miles, and J. Hunter, *J. Electrochem. Soc.*, **120**, 1441 (1973).

64. J. Schoonman, *J. Electrochem. Soc.*, **123**, 1772 (1976).

65. J. Schoonman and A. Wolfert, *Solid State Ionics*, **3–4**, 373 (1981).

66. M. A. Reddy and M. Fichtner, *J. Mater. Chem.*, **21**, 17059 (2011).

67. H. Konishi, T. Minato, T. Abe, and Z. Ogumi, *J. Electrochem. Soc.*, **164**, A3702 (2017).

68. V. K. Davis, C. M. Bates, K. Omichi, B. M. Savoie, N. Momčilović, Q. Xu, W. J. Wolf, M. A. Webb, K. J. Billings, N. H. Chou, S. Alayoglu, R. K. McKenney, I. M. Darolles, N. G. Nair, A. Hightower, D. Rosenberg, M. Ahmed, C. J. Brooks, T. F. Miller, III, R. H. Grubbs, and S. C. Jones, *Science*, **362**, 1144 (2018).

69. H. Konishi, T. Minato, T. Abe, and Z. Ogumi, *J. Appl. Electrochem.*, **48**, 1205 (2018).

70. H. Konishi, T. Minato, T. Abe, and Z. Ogumi, *J. Phys. Chem. C*, **123**, 10246 (2019).

71. K. Okazaki, Y. Uchimoto, T. Abe, and Z. Ogumi, *ACS Energy Lett.*, **2**, 1460 (2017).

72. T. Yamanaka, K. Okazaki, T. Abe, K. Nishio, and Z. Ogumi, *ChemSusChem*, **12**, 527 (2019).

73. R. Hagiwara, T. Hirashige, T. Tsuda, and Y. Ito, *J. Fluorine Chem.*, **99**, 1 (1999).

74. T. Enomoto, Y. Nakamori, K. Matsumoto, and R. Hagiwara, *J. Phys. Chem. C*, **115**, 4324 (2011).

75. R. Hagiwara, T. Hirashige, T. Tsuda, and Y. Ito, *J. Electrochem. Soc.*, **149**, D1 (2002).

76. R. Hagiwara and J. S. Lee, *Electrochemistry*, **75**, 23 (2007).

77. T. Yamamoto, K. Matsumoto, R. Hagiwara, and T. Nohira, *ACS Appl. Energy Mater.*, **2**, 6153 (2019).

78. K. Matsumoto, R. Hagiwara, and Y. Ito, *Electrochem. Solid-State Lett.*, **7**, E41 (2004).

79. T. Yamamoto, K. Matsumoto, R. Hagiwara, and T. Nohira, *J. Electrochem. Soc.*, **168**, 040530 (2021).